









Cite this: *Phys. Chem. Chem. Phys.*,  
2023, 25, 32430

# Morphology and hygroscopicity of nanoplastics in sea spray†

Sarah Suda Petters,  <sup>‡\*</sup><sup>a</sup> Eva Rosendal Kjærgaard,  <sup>a</sup> Freja Hasager,  <sup>a</sup>  
 Andreas Massling,  <sup>b</sup> Marianne Glasius  <sup>a</sup> and Merete Bilde  <sup>\*a</sup>

The role of airborne nanoparticles in atmospheric chemistry and public health is largely controlled by particle size, morphology, surface composition, and coating. Aerosol mass spectrometry provides real-time chemical characterization of submicron atmospheric particles, but analysis of nanoplastics in complex aerosol mixtures such as sea spray is severely limited by challenges associated with separation and ionization of the aerosol matrix. Here we characterize the internal and external mixing state of synthetic sea spray aerosols spiked with 150 nm nanoplastics. Aerosols generated from pneumatic atomization and from a sea spray tank are compared. A humidified tandem differential mobility analyzer is used as a size and hygroscopicity filter, resulting in separation of nanoplastics from sea spray, and an inline high-resolution time-of-flight aerosol mass spectrometer is used to characterize particle composition and ionization efficiency. The separation technique amplified the detection limit of the airborne nanoplastics. A salt coating was found on the nanoplastics with coating thickness increasing exponentially with increasing bulk solution salinity, which was varied from 0 to 40 g kg<sup>-1</sup>. Relative ionization efficiencies of polystyrene and sea salt chloride were 0.19 and 0.36, respectively. The growth-factor derived hygroscopicity of sea salt was 1.4 at 75% relative humidity. These results underscore the importance of separating airborne nanoplastics from sea salt aerosol for detailed online characterization by aerosol mass spectrometry and characterization of salt coatings as a function of water composition. The surface coating of nanoplastic aerosols by salts can profoundly impact their surface chemistry, water uptake, and humidified particle size distributions in the atmosphere.

Received 8th August 2023,  
Accepted 10th November 2023

DOI: 10.1039/d3cp03793b

rsc.li/pccp

## 1 Introduction

The environmental detection, fate, and transport of micro- and nanoplastics are of great interest in environmental chemistry, atmospheric chemistry, and public health.<sup>1,2</sup> The presence of microplastics (diameter < 5 mm) in living tissue suggests a strong potential for numerous adverse health effects.<sup>3–5</sup> Plastic waste accumulates in the ocean, where weathering, oxidation, and biological processes convert larger plastics into micro- and nanoplastics (having at least one spatial dimension between 1 and 1000 nm;<sup>6,7</sup> sometimes defined as ≤100 nm<sup>8–10</sup>).<sup>11–14</sup> Plastic buoyancy in the water column changes with degradation and surface fouling,<sup>12</sup> and nanoplastics at the water surface can

be transferred to the air with sea spray through wave-breaking and bubble bursting.<sup>14,15</sup> Microplastics have been found in the remote marine atmosphere and in cloud water.<sup>14,16</sup> The low mass concentration of nanoplastics relative to sea salt, as well as organic or inorganic coatings on nanoplastic aerosols, are significant challenges for studies investigating the mechanism of nanoplastic aerosolization at the air–sea interface.<sup>15</sup>

Both plastic and sea salt particles can be detected by size-resolved aerosol mass spectrometry, which provides real-time bulk chemical characterization of submicron atmospheric aerosols.<sup>17,18</sup> However, the analysis of nanoplastics in complex aerosol mixtures such as sea spray is limited by challenges associated with ionization and speciation of the aerosol matrix.<sup>19,20</sup> Furthermore, the role of airborne nanoparticles in atmospheric chemistry and public health is strongly influenced by physico-chemical properties including particle size,<sup>4,15,21,22</sup> shape,<sup>23–25</sup> and coatings.<sup>26–29</sup>

Sea salt coating on nanoplastic aerosol can impact water uptake and cloud droplet nucleation efficiency as well as surface chemistry and size distribution dynamics. In this work we characterize the internal and external mixing state, hygroscopicity, and ionization efficiency of sea spray aerosols spiked

<sup>a</sup> Department of Chemistry, Aarhus University, DK-8000 Aarhus C, Denmark.

E-mail: [bilde@chem.au.dk](mailto:bilde@chem.au.dk), [sarah.petters@ucr.edu](mailto:sarah.petters@ucr.edu)

<sup>b</sup> Department of Environmental Science, Aarhus University, DK-4000 Roskilde, Denmark

† Electronic supplementary information (ESI) available: Supplemental methods and tables. See DOI: <https://doi.org/10.1039/d3cp03793b>

‡ Present address: Bourns College of Engineering Center for Environmental Research and Technology, University of California Riverside, Riverside, CA 92507, USA.

with 150 nm polystyrene latex spheres. A humidified tandem differential mobility analyzer (HTDMA) is used as a size and hygroscopicity filter, separating the nanoplastic particles from the sea spray, and an inline high-resolution time-of-flight aerosol mass spectrometer (HR-ToF-AMS) is used to determine particle composition. The hygroscopicity of sea salt and the coating of sea salt on nanoplastics are characterized. The relative ionization efficiency of sea salt chloride and polystyrene are investigated by comparing the high-resolution AMS spectra to the HTDMA mass measurements. This work shows the relationship between salinity and sea salt coatings on nanoplastic particles and presents a novel separation method for the online detection and physico-chemical characterization of microplastic and nanoplastic particles in externally mixed aerosols.

## 2 Methods

### 2.1 Sample preparation

The following reagents were used without additional purification: NaCl (Sigma-Aldrich,  $\geq 99.5\%$ , lot #STBK1847);  $\text{MgCl}_2 \cdot 6\text{H}_2\text{O}$  (Sigma BioXtra,  $\geq 99.0\%$ ; lot #BCCG7484);  $\text{Na}_2\text{SO}_4$  (Sigma,  $\geq 99.0\%$ , lot #MKCM5983);  $\text{CaCl}_2$  (Sigma BioUltra,  $\geq 99.5\%$ , #BCCD5465);  $\text{K}_2\text{SO}_4$  (Sigma,  $\geq 99.0\%$ , #MKBR1323V);  $\text{KNO}_3$  (Sigma ACS Reagent,  $\geq 99.0\%$ , lot #MKBR7577V); NaBr (Sigma ACS Reagent,  $\geq 99.0\%$ , lot #MKBP5844V); MilliQ water ( $\geq 18.2 \text{ M}\Omega \text{ cm}$  resistivity at  $25^\circ\text{C}$ , 2 ppb total organic carbon, EMD Millipore); aqueous polystyrene latex spheres (PSL) of diameter  $147 \pm 3 \text{ nm}$ , stock solution containing trace amounts of dispersant and of sodium azide (Thermo Scientific NIST traceable, 3051A, lot #39009).

Synthetic sea salt containing  $\text{Cl}^-$ ,  $\text{Na}^+$ ,  $\text{SO}_4^{2-}$ ,  $\text{K}^+$ ,  $\text{Ca}^{2+}$ ,  $\text{Br}^-$ ,  $\text{Mg}^{2+}$ , and  $\text{NO}_3^-$  with mass contributions relative to  $\text{Cl}^-$  of 1.00, 0.56, 0.14,  $1.7 \times 10^{-2}$ ,  $2.2 \times 10^{-2}$ ,  $3.1 \times 10^{-3}$ ,  $6.8 \times 10^{-2}$ , and  $2.6 \times 10^{-3}$ , respectively, was prepared following Nielsen and Bilde<sup>30</sup> and diluted in MilliQ water following a logarithmically-spaced salinity ramp from 40 to  $8 \times 10^{-5} \text{ g kg}^{-1}$ , with additional samples having salinity between 0.6 and  $0.15 \text{ g kg}^{-1}$  (Table 1). Solutions were spiked with 0.15 to  $0.18 \text{ mg kg}^{-1}$  PSL, diluted from stock solution containing 1% solids by mass.

Aerosol containing sea salt and PSL was generated either by atomization or by bubble bursting. Atomization experiments used a Collison atomizer (TSI 3076) at room temperature with a constant liquid flow of  $0.4 \text{ mL min}^{-1}$  (provided by a syringe pump) and an air flow of  $3 \text{ L min}^{-1}$  (Table S1, ESI,† lines 1–66). Bubble bursting experiments were performed using the ÆGOR sea spray tank holding 20 L of temperature-controlled solution, held at  $20^\circ\text{C}$ , that was bubbled with  $3.35 \text{ L min}^{-1}$  of clean air from a glass frit placed at the tank bottom (Table S1, ESI,† lines 67–107).<sup>31–33</sup> These experiments were carried out as part of a campaign described in more detail by Kjærgaard *et al.*<sup>15</sup> For all experiments, clean pressurized air from the in-house air handling system was supplied through an air purifier at 35 psi (TSI 3074B), and the mass flow rate was actively held steady by a mass flow controller (Vögtlin Instruments). Aerosol was

Table 1 Solutions prepared for aerosol generation

# <sup>a</sup>	Salinity <sup>b</sup> ( $\text{g kg}^{-1}$ )	PSL <sup>c</sup> ( $\text{mg kg}^{-1}$ )
A	41	0.18
1	6.21	0.18
2	0.94	0.18
3	0.14	0.18
4	0.022	0.18
5	$3.27 \times 10^{-3}$	0.18
6	$4.96 \times 10^{-4}$	0.18
7	$7.52 \times 10^{-5}$	0.18
8	0	0.18
2a	0.596	0.18
2b	0.378	0.18
2c	0.239	0.18
2d	0.151	0.18
MilliQ	0	0
ÆGOR 1	0	0.15
ÆGOR 2	0.01	0.15
ÆGOR 2	0.01	0.15
ÆGOR 3	0.0215	0.15
ÆGOR 4	0.0464	0.15
ÆGOR 5	0.1	0.15
ÆGOR 6	0.2154	0.15
ÆGOR 7	0.464	0.15
ÆGOR 8	1	0.15
ÆGOR 9	0	0

<sup>a</sup> Unless otherwise indicated, solutions were atomized using a Collison atomizer. ÆGOR solutions were aerosolized *via* bubble bursting using the ÆGOR sea spray tank.<sup>15,31–33</sup> <sup>b</sup> Salinity is the total synthetic sea salt mass mixing ratio in water. <sup>c</sup> Polystyrene latex nanosphere mass mixing ratio in water,  $147 \pm 3 \text{ nm}$ , Thermo Scientific Lot #39009; NIST traceable. An experiment list is found in Table S1 (ESI).

dried to below 7% relative humidity (RH) using two inline silica gel diffusion dryers.

### 2.2 Instrumentation

Fig. 1 shows the instrument schematic downstream of sample generation. Particles in the aerosol stream were size-selected, humidified, and separated using a hygroscopicity tandem differential mobility analyser (HTDMA). The fractionated particle stream was routed to a high-resolution time-of-flight aerosol mass spectrometer (HR-ToF-AMS; Aerodyne,<sup>17</sup> hereafter, AMS). The instrumentation was operated in three modes: scanning electrical mobility spectrometer mode (SEMS mode; Brechtel Model 2002; Fig. 1, elements A and B-1); HTDMA mode (Fig. 1, elements A, B-2, C, and D-1); and HTDMA-AMS mode (Fig. 1, elements A, B-2, C, D-2, and E). The inset (F) depicts the fractionation of particles from an externally mixed aerosol upstream of AMS analysis. In a typical set of experiments, the aerosol size distribution was measured in SEMS mode, flows were optimized in HTDMA mode based on the observed signal-to-noise ratio, the HTDMA scan duration setting was extended, and the instrument was physically reconfigured for measurement in HTDMA-AMS mode.

The HTDMA (Brechtel Model 3002) described by Lopez-Yglesias *et al.*<sup>34</sup> was used as in prior work.<sup>35,36</sup> An impactor at the inlet removed particles larger than  $1 \mu\text{m}$  in diameter. The polydisperse dry aerosol was then returned to an equilibrium charge distribution by an X-ray-based neutralizer (Fig. 1, element A). DMA 1 was scanned between 5 and  $1000 \text{ nm}$  (SEMS mode) or

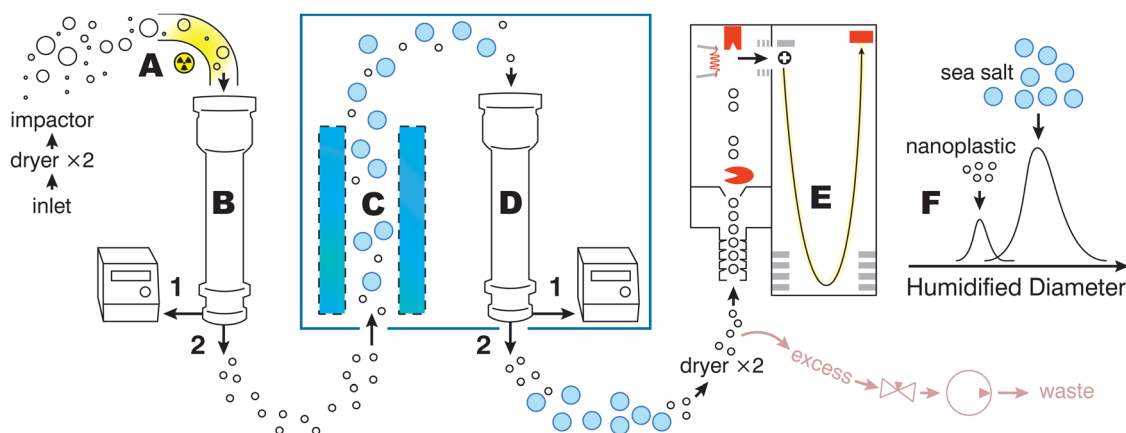


**Fig. 1** HTDMA-AMS instrument schematic. Dry polydisperse aerosol is generated upstream by either an atomizer or the  $\text{ÆGOR}$  sea spray tank, is dried, and then particles larger than  $1\ \mu\text{m}$  are removed by an impactor. Polydisperse dry sample aerosol is represented by open circles. Flows are varied and are described in the text. (A) X-Ray-based charge neutralizer, (B) first differential mobility analyzer operated as a scanning electrical mobility analyzer (SEMS) with a mixing condensation particle counter (MCPC) as its detector (path 1), or in single-size selection mode (path 2). (C) Humidification and (D) second DMA operated as a humidified scanning electrical mobility analyzer (HSEMS) with an MCPC detector (path 1), or as a scanning humidified-size selector (path 2). Path 2 includes a pump and needle valve to adjust sample flow out of the DMA. (E) High-resolution aerosol time-of-flight mass spectrometer (HR-ToF-AMS) consisting of an aerodynamic lens, a chopper, flash vaporization and electron impact ionization, and a time-of-flight mass analyzer operated in single-reflection mode. (F) Schematic showing how the aerosol is separated into more- and less-hygroscopic particles for real-time analysis.

held at  $150\ \text{nm}$  (HTDMA and HTDMA-AMS modes) with a sample flow of  $0.5$  to  $1\ \text{L}\ \text{min}^{-1}$  and a sheath flow of  $3$ ,  $5$ , or  $6.5\ \text{L}\ \text{min}^{-1}$ . Sheath and sample flows were set as needed to increase peak height (by using a larger sample flow) while maintaining narrow peaks (by increasing the sheath/sample flow ratio), within instrumental limits. The humidifier and DMA 2 (Fig. 1, elements C and D) were held at a stable RH of  $75\%$ . DMA 2 scanned from  $75$  to  $500\ \text{nm}$  or from  $100$  to  $400\ \text{nm}$  with a sheath flow of  $5\ \text{L}\ \text{min}^{-1}$  and a sample flow of  $0.5\ \text{L}\ \text{min}^{-1}$ . Typical HTDMA scans lasted  $2$ – $3$  min. Table S1 (ESI $^\dagger$ ) includes the experiment list as well as scan settings and measured parameters for each experiment.

The AMS assisted in confirming the transmission of nanoplastic aerosols through the HTDMA and in characterizing the relative ionization efficiency of both polystyrene and NaCl. In HTDMA-AMS mode (Fig. 1, element D-2), the aerosol exited DMA 2 and flowed to the AMS at  $0.15\ \text{L}\ \text{min}^{-1}$ , passing through two diffusion dryers before being split between an excess flow to waste ( $0.05\ \text{L}\ \text{min}^{-1}$  controlled by an external pump in combination with needle valve) and a sample flow to the AMS inlet ( $0.1\ \text{L}\ \text{min}^{-1}$ ), verified daily. The flow was laminar with a minimal pressure drop. A delay of  $80\ \text{s}$  between the instruments was found by calibrating the alignment between data streams in independent tests. This corresponds to a flow of  $0.15\ \text{L}\ \text{min}^{-1}$  through  $4\ \text{m}$  of  $3/16''$  (inner diameter) tube,  $0.15\ \text{L}\ \text{min}^{-1}$  through  $1\ \text{m}$  of  $1/2''$  tube (corresponding to two dryers), and after the split,  $0.1\ \text{L}\ \text{min}^{-1}$  through  $0.5\ \text{m}$  of  $3/16''$  tube.

In the AMS, particles passed through an aerodynamic lens, a spinning chopper, and a  $0.295\ \text{m}$  long particle time-of-flight zone. The particle beam was impacted on the heated vaporizer and the resultant gas was ionized *via* electron ionization at  $70\ \text{eV}$ . Radical cations then passed *via* ion optics into the time-of-flight mass analyser operated in single-reflection mode (“V”-mode, path length  $1.3\ \text{m}$ ,  $m/z\ 9$ – $409$ )<sup>17</sup> with an average

resolving power  $m/\Delta m$  of  $2500$  during the experiments (Table S2, ESI $^\dagger$ ). The upstream HTDMA scans were increased in duration to  $2\ \text{h}$  (Table S1, ESI $^\dagger$ ) to increase the diameter resolution for the AMS, which reports a mass spectrum every  $1\ \text{min}$ .

Fig. 2 shows the AMS vaporizer characterization. The vaporizer temperature was raised from its typical value of  $615\ ^\circ\text{C}$  to  $811 \pm 20\ ^\circ\text{C}$  to allow faster desorption of plastics and salts.<sup>18</sup> The temperature was controlled by adjusting the current setting to between  $70$  and  $100\%$  of the maximum value of  $\sim 1.28\ \text{A}$ . Temperature is characterized as a function of the power provided across the resistive element because the temperature probe may come loose and provide erroneously low values.<sup>37,38</sup>

Fig. 2, panel A shows the vaporizer current as a function of the control box setting. The vaporizer current of this instrument (at Aarhus University) is typically set to  $0.93\ \text{A}$  (‘setting 80,’ *i.e.*,  $80\%$  of the maximum) during measurements and in standby mode. In-house tests with ammonium nitrate indicated that this corresponds to a temperature of  $\sim 600\ ^\circ\text{C}$ , recommended by Williams<sup>37</sup> for standard operation. Following Ovadnevaite *et al.*,<sup>18</sup> the current was raised to  $1.19\ \text{A}$  (‘setting 95,’ *i.e.*,  $95\%$  of the maximum) to encourage complete and fast evaporation of sea salt. We also found that the higher temperature was beneficial for measuring plastics.

In Fig. 2, panels B and C show the vaporizer temperature as a function of current and power. The AMS vaporizer temperature-setting relationship was found using the temperature coefficient of resistance. Power ( $P$ ), current ( $I$ ), and voltage ( $V$ ) were characterized at setting 80 and 95 (Table S3, ESI $^\dagger$ ). Resistance ( $R$ ) was found *via*  $R = V/I$ . The temperature dependence of resistance of a fixed-size element is  $R = R_0(1 + \alpha(T - T_0))$ , where  $\alpha$  is the temperature coefficient of resistance,  $R_0$  is the resistance at temperature  $T_0$ , and  $R$  is the resistance at a new

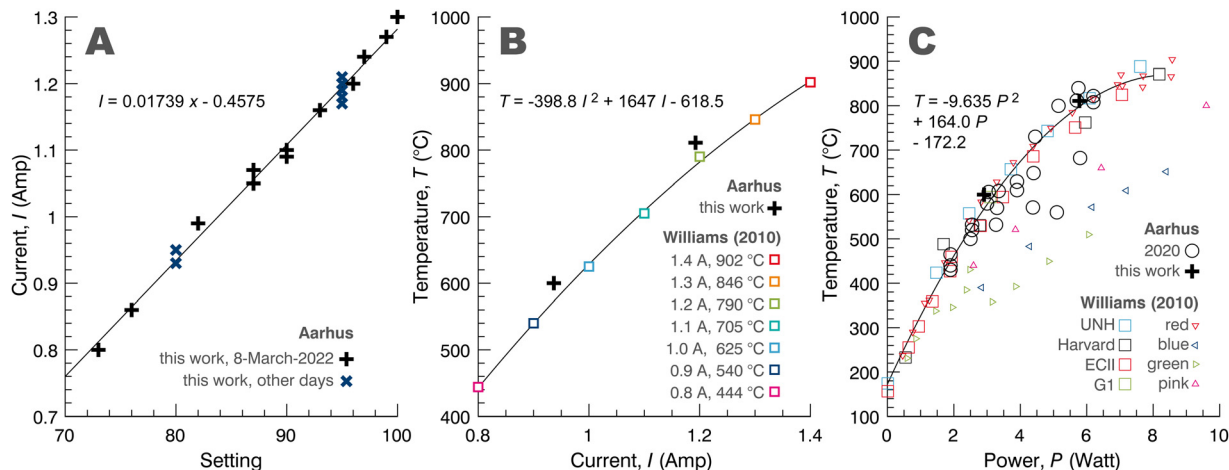


Fig. 2 Vaporizer characterization for the Aarhus University high-resolution time-of-flight aerosol mass spectrometer (HR-ToF-AMS; Aerodyne 2018). (A) Vaporizer current as a function of instrument setting. (B) Vaporizer temperature as a function of current, calculated for this work (black) and compared to the data presented by Williams (2010) for the Xiamen quadrupole aerosol mass spectrometer. (C) Vaporizer temperature as a function of power for several instruments (Williams 2010; square symbols are from her second slide, triangle symbols labeled with original colors are presented in her third slide). The line represents a fit to the Williams data. Prior temperature measurements (black circles) are compared to the values of this work (black crosses). A known issue wherein the temperature probe can become loose affects some of these data points. Data are given in Table S3 (ESI<sup>†</sup>).

temperature  $T$ . After rearrangement we can solve for the unknown vaporizer temperature at setting 95:

$$T_{95} = T_{80} + \frac{1}{\alpha} \left( \frac{R_{95}}{R_{80}} - 1 \right) \quad (1)$$

where subscripts indicate the vaporizer setting (80 or 95). The  $T_{80}$  was generally very close to 600 °C (probe temperature reading of 615 °C), and the value of  $\alpha$  for pure tungsten is 0.0045 °C<sup>-1</sup>;  $R_{80}$  and  $R_{95}$  were 3.29 and 4.08 Ω, respectively (Table S3, ESI<sup>†</sup>). For the porous tungsten inverted cone vaporizer, we multiply  $\alpha$  by a factor of 0.25 based on the measurements of Williams<sup>37</sup> and prior calibrations at Aarhus University (Fig. 2, panel C). The adjusted  $T_{95}$  is then 811 °C. We estimate an uncertainty of ±20 °C based on the scatter in the Williams data.

### 2.3 Data processing and calculations

Data streams from DMA 1, DMA 2, and the AMS were aligned and combined during analysis. Alignment is based on a fixed 80 s delay between instruments, as in past work.<sup>34,39</sup> The DMA 1 and DMA 2 alignment is built into the HTDMA software based on user calibration.<sup>34</sup> For the HTDMA-AMS alignment, the exponential diameter scan of DMA 2 was mapped onto a time axis based on the scan's start and stop times ( $\log_{10}D$  is linear with scan time and can be interpolated onto a new time axis<sup>40</sup>). The HTDMA times at 1 Hz resolution were interpolated onto the AMS times (at a much lower resolution of about 1 min<sup>-1</sup>). The AMS signal is then displayed as a function of the HTDMA-selected mobility diameter.

An inversion algorithm is used to determine the value of  $D$  associated with each peak in the humidified diameter scan (Fig. S1, ESI<sup>†</sup>).<sup>41,42</sup> The hygroscopic growth factor, GF, is calculated as the ratio  $D/D_{\text{dry}}$ , where  $D$  is the humidified diameter and  $D_{\text{dry}}$  is the dry diameter. The inversion algorithm fits the raw instrument response function (concentration vs.

electrical mobility) using a GF probability distribution based on a forward model that accounts for the upstream aerosol size distribution and its transfer through the HTDMA. A two-component model was used, corresponding to a bimodal GF distribution. The shape of the humidified size distribution is governed by the width of the transfer functions, not necessarily by a broad distribution of hygroscopicity values.<sup>15,42</sup> The inversion accounts for the transfer function and the effect of particle charging, including multiply charged particles. The algorithm returns the GF and number fractions of the more- and less-hygroscopic modes, corresponding to sea salt and to PSL. (An example is shown in Fig. S1, ESI<sup>†</sup>).

The coating thickness of salt on PSL particles was determined using the growth factor of PSL,  $GF_{\text{PSL}}$ . The wet volume of the coated PSL particles was found *via*:

$$V_{\text{wet}} = \frac{\pi}{6} (GF_{\text{PSL}} \times D_{\text{dry,PSL}})^3 \quad (2)$$

The volume of salt water enveloping the PSL at 75% RH was determined *via*

$$V_{\text{sw}} = V_{\text{wet}} - \frac{\pi}{6} D_{\text{dry,PSL}}^3 \quad (3)$$

Here  $V_{\text{sw}} = V_{\text{s}} + V_{\text{w}}$ ,  $V_{\text{s}}$  is the dry sea salt volume, and  $V_{\text{w}}$  is the water volume dissolving the salt. The hygroscopicity relation proposed by Petters and Kreidenweis<sup>43</sup> describes the fixed ratio of solute to water as a function of the activity of water ( $a_{\text{w}}$ ) *via*  $a_{\text{w}}^{-1} = 1 + \kappa V_{\text{s}} V_{\text{w}}^{-1}$ , which can be rearranged as follows:

$$V_{\text{s}} = V_{\text{sw}} \left( \frac{1 - a_{\text{w}}}{a_{\text{w}}(\kappa - 1) + 1} \right) \quad (4)$$

The hygroscopicity parameter of the sea salt mixture (Section 2.1),  $\kappa$ , was found using the measured growth factor of sea salt at 75% RH *via*  $\kappa = a_{\text{w}}^{-1} (GF^3 - 1) (1 - a_{\text{w}})^{43-45}$



To calculate a coating thickness, the dry, coated PSL volume is used:

$$V_{\text{dry,coated}} = V_s + \frac{\pi}{6} D_{\text{PSL}}^3 \quad (5)$$

$$D_{\text{dry,coated}} = \left( \frac{6}{\pi} V_{\text{dry,coated}} \right)^{1/3} \quad (6)$$

The coating thickness ( $\tau$ ) is then  $\tau = (D_{\text{dry,coated}} - D_{\text{dry,PSL}})/2$ .

The size of generated droplets prior to any water evaporation was calculated using the salinity of the aerosolized stock solutions. For droplets containing PSL, the volume of the salt coating,  $V_s$ , calculated in eqn (4) was used to find the mass of salt *via*  $m_s = V_s \rho_s$  (where  $m_s$  is the mass of salt and  $\rho_s$  is the density of salt,  $2.16 \text{ g cm}^{-3}$ ). The volume of water is then  $V_w = m_s / (s \rho_w)$  (where  $s$  is salinity expressed in  $\text{kg kg}^{-1}$  and  $\rho_w$  is the density of water). The droplet volume is  $V_{\text{drop}} = V_w + V_s + V_{\text{PSL}}$ , where  $V_{\text{PSL}}$  is the volume of the clean and dry (un-coated) PSL particle, and the resulting droplet diameter is

$$D_{\text{drop}} = \left( \frac{6}{\pi} V_{\text{drop}} \right)^{1/3} \quad (7)$$

The AMS data analysis is described in detail in Section S3 (ESI<sup>†</sup>). Briefly, unit-mass AMS data were analysed using ToF-AMS Analysis Toolkit 1.65C (Squirrel 1.65C; mass calibration, air beam correction, background subtraction, and mass spectra with unit  $m/z$  resolution).<sup>17,46</sup> High-resolution mass spectra were obtained using ToF-AMS HR Analysis 1.25C (Pika 1.25C; peak shape factor analysis and data export) and MATLAB 2021a (high-resolution fitting following Corbin *et al.*<sup>47</sup> and Sueper *et al.*<sup>46</sup>). High-resolution fitting was performed for sea salt and polystyrene ions. Sea salt ions analyzed included  $^{35}\text{Cl}$ ,  $\text{H}^{36}\text{Cl}$ ,  $^{37}\text{Cl}$ ,  $\text{H}^{37}\text{Cl}$ , and  $\text{Na}^{35}\text{Cl}$  (following, *e.g.*, Ovadnevaite *et al.*<sup>18</sup>) and polystyrene ions analyzed included  $m/z$  104 (corresponding to the radical cation  $\text{C}_8\text{H}_8^{\bullet+}$ ),<sup>48</sup> 103, and 78.<sup>49,50</sup> The  $m/z$  values obtained by high-resolution ToF fitting are tabulated in Section S3, Tables S5 and S6 (ESI<sup>†</sup>).

The particle time-of-flight (PToF) measurement of the AMS was used to calculate the vacuum aerodynamic diameter ( $D_{\text{va}}$ ). The airbeam-subtracted unit-mass data were used. The PToF particle velocity was converted to  $D_{\text{va}}$  *via* eqn (S6) in Section S3 (ESI<sup>†</sup>). The Jayne shape factor,  $S$ , was calculated *via*

$$S = D_{\text{va}}/D_{\text{mob}} \times \rho_0/\rho_m \quad (8)$$

where  $D_{\text{mob}} = 150 \text{ nm}$  is the mobility diameter selected by the DMA,  $\rho_0$  is unit density, and  $\rho_m$  is the bulk material density (using  $2.16$  and  $1.054 \text{ g cm}^{-3}$  for sea salt and PSL, respectively).<sup>51,52</sup>

Understanding of the ionization efficiency of the nanoplastics is important because the AMS is often used in the field to detect and characterize unknown aerosols without the aid of an upstream HTDMA for mass concentration verification. In the future we hope to distinguish between different types of plastics. Further, it is important to know the ionization efficiency of sea salt for comparison with a limited number of other studies quantifying NaCl using electron ionization.

Ionization efficiency (IE) and relative ionization efficiency (RIE) were calculated for chloride and polystyrene by comparing the HTDMA mass measurement to the AMS mass spectra. Collection efficiency was set to 0.25 for both the salt and the salt-coated PSL, following the recommendation of Ovadnevaite *et al.*<sup>18</sup> for dry salts. Details are given in Section S4 (ESI<sup>†</sup>).

## 3 Results and discussion

### 3.1 Separation of sea salt and plastic particles

Fig. 3 shows the separation of 147 nm nanoplastics from sea salt particles of the same dry size for samples generated using an atomizer. Dry size selection was performed at 150 nm. Panel A shows the nanoplastic in the absence of salt, and panels B–F illustrate the effect of adding synthetic sea salt to the solution prior to atomization. Growth factors are tabulated in Table S10 (ESI<sup>†</sup>).

The PSL peak remained distinct from the sea salt, disappearing at a salinity of between 1 and  $6 \text{ g kg}^{-1}$  (Fig. 3, panels E and F). Even with  $6.21 \text{ g kg}^{-1}$  of sea salt, a distortion in the humidified size distribution near 150 nm can be attributed to PSL, despite the 350-fold increase in salt mass relative to the  $18 \text{ mg kg}^{-1}$  of PSL in panel F. The PSL and sea salt peaks are of similar magnitude in Fig. 3, panels B and C, where the sea salt concentration is  $1.2\times$  and  $7.8\times$  larger than that of PSL, respectively.

Fig. 4 shows the separation of nanoplastics and sea salt for samples generated using the ÆGOR sea spray tank. Though fewer particles were generated by the tank method, the separation of salt from plastic is still evident. The growth factor of sea salt was  $\text{GF}_s = 1.74$ . The growth factor of the PSL particles was

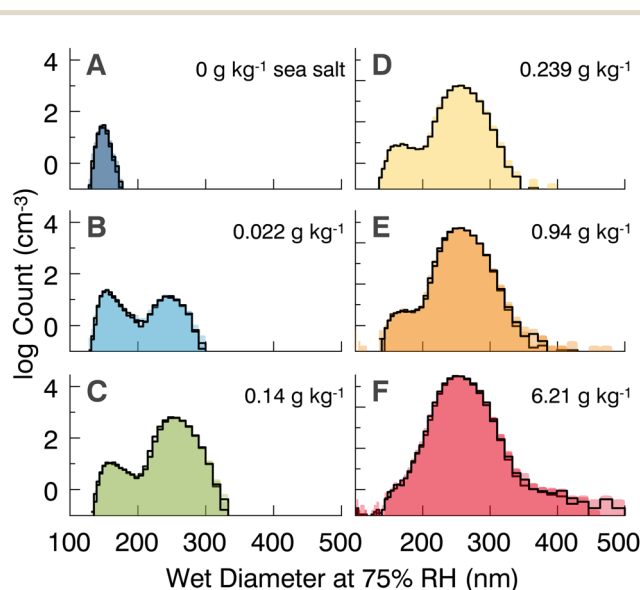


Fig. 3 Size distributions of humidified 147 nm particles at 75% RH. Atomized stock solutions contained  $0.18 \text{ mg kg}^{-1}$  of 147 nm polystyrene latex spheres and varying sea salt concentration. Sea salt concentrations are printed in  $\text{g salt per kg water}$ . Note that the size distributions are not inverted and have units of particles per  $\text{cm}^3$ . (Experiments: (A) 1, 2, 19; (B) 9, 27; (C) 11, 30; (D) 44, 58; (E) 14, 31; (F) 15, 34; found in Table S1, ESI<sup>†</sup>).

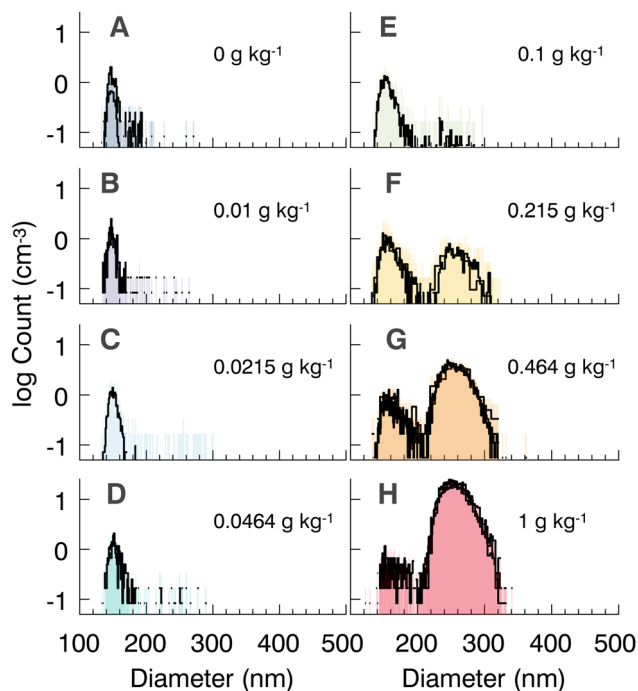


Fig. 4 Size distributions of humidified 147 nm particles at 75% RH. Particles were generated using the ÆGOR sea spray tank. (Experiments: (A) 69, 71; (B) 74, 76; (C) 80; (D) 83, 84; (E) 86; (F) 91, 92; (G) 95, 96, 98; (H) 99, 101, 103; found in Table S1, ESI†). Note that the size distributions are not inverted and have units of particles per  $\text{cm}^3$ .

near 1 but increased as particles became coated with salt as salinity was raised. Only after humidified separation by the HTDMA instrument is the plastic peak apparent. Growth factors are tabulated in Table S10 (ESI†). Note that the nanoplastics used in this study are assumed to be spherical before acquiring a coating of dried salt. Microplastics have been observed to be highly irregular in shape, though the shape of nanoplastics may be more spherical due to different formation mechanisms.<sup>53</sup> Irregularly shaped particles have different aerodynamic drag, and can be perceived differently in both the HTDMA and AMS instruments due to their larger mobility diameter and due to beam broadening in the AMS. This must be addressed in future studies of irregularly shaped nano- and microplastics.

Our experiments explore a reasonable range of salinities representative of a range of conditions from freshwater to concentrated ocean water, with similar plastic concentrations in each experiment. The salinity of the global oceans is generally near  $35 \text{ g kg}^{-1}$  but varies with the input of rivers; in the Aarhus Bay, for example, it is about  $19 \text{ g kg}^{-1}$ .<sup>54</sup> Because runoff is a source of plastic pollution,<sup>53</sup> we can expect that sometimes an enhanced concentration of nanoplastic particles will coincide with lower salinity. Van Sebille *et al.*<sup>55</sup> provide an estimate of microplastic mass in the global oceans; extending their surface density of microplastics (diameter < 5 mm) to a depth of 1 m, we estimate a maximum concentration of microplastics of  $0.1 \text{ mg kg}^{-1}$  of ocean water. The concentration of nanoplastics at the ocean surface is not well known, but microplastics

have been detected in the marine boundary layer mixed with sea spray<sup>13,14</sup> and spectroscopically matched with the plastics found in the waves below.<sup>14</sup> The concentration of nanoplastics added to our solutions ( $0.15\text{--}0.18 \text{ mg kg}^{-1}$ ; Table 1) is close to the upper estimate for microplastics provided by van Sebille.<sup>54</sup>

Note that particle concentration in Fig. 3 and 4 is not inverted, meaning that only the charged particles that passed all the way through the HTDMA are reported (Fig. 1, route A, B, C, D-1). Raw counts per bin are converted to units of particles per  $\text{cm}^3$  ( $dN/dD$ , rather than  $dN/d \log_{10} D$ ;  $N$  is the number of particles). The count on the y-axis can therefore be compared directly to the downstream AMS signal without dividing by  $\log_{10}(\Delta D)$ .

Fig. S4 in the ESI,† overlays the upstream polydisperse aerosol and the separated salt and plastic downstream using the HTDMA. These data correspond to the atomizer experiments shown in Fig. 3. As salinity increases, the PSL peak disappears from the dry size distribution measured prior to the HTDMA. A similar trend was observed as salinity was increased in the ÆGOR experiments performed by Kjærsgaard *et al.*,<sup>15</sup> which were run in parallel to the experiments shown in Fig. 4.

### 3.2 Sea salt growth factor and hygroscopicity

The physical/chemical characterization of nanoplastic-containing sea salt aerosol is strongly influenced by the presence and water uptake of the salts. Fig. 5 shows the hygroscopic water uptake (panel A) and corresponding growth factor derived  $\kappa$  values (panel B) for sea salt aerosols in the context of other measurements and models.<sup>43,56–59</sup> Data are plotted as a function of  $a_w$  to remove the diameter dependence of RH (*i.e.*, the Kelvin term); here,  $\text{RH} \sim a_w \times 100\%$ . The atomizer-generated sea salt aerosol of Zieger *et al.*<sup>56</sup> was more hygroscopic than that of this work. Zieger *et al.*<sup>56</sup> include a comparison of atomizer-generated sea salt to atomizer-generated NaCl, showing NaCl to be slightly more hygroscopic than sea salt. The results of Rosati *et al.*<sup>44</sup> (not shown) also suggest NaCl is more hygroscopic than sea salt, and the Aerosol Inorganics Model (AIM)<sup>57,60</sup> is in agreement (the solid green line is NaCl, the dotted line is sea salt;  $\text{Br}^-$  is replaced in the model by  $\text{Cl}^-$ ). The spread in atomizer-generated sea salt  $\kappa$  in this work is 1.4–1.8 at an  $a_w$  of 0.75, slightly lower than the AIM model for sea salt  $\kappa$ .

Sea spray tank-generated aerosols had greater diversity between studies. The tank-generated sea salt aerosol of Wex *et al.*<sup>58</sup> had  $\kappa$  values as high as 1.85 at an  $a_w$  of 0.75. These measurements were very close to the prediction made by AIM<sup>57,60</sup> for NaCl, and were the highest of the measured  $\kappa$  values shown in Fig. 5. The ÆGOR tank-generated sea salt aerosol (this work) was less hygroscopic, and the tank-generated sea salt aerosol of Zieger *et al.*<sup>56</sup> was the least hygroscopic measurement in this comparison, with a  $\kappa$  of 1.32 at an  $a_w$  of 0.75. The mechanism of aerosolization can be an important control of the resulting aerosol physicochemical properties.

Fig. 5 also compares the aerosols generated by atomization to those generated by a sea spray tank. The range of hygroscopicity observed for atomizer-generated overlaps with the range observed for tank-generated sea salt aerosols. Growth factor

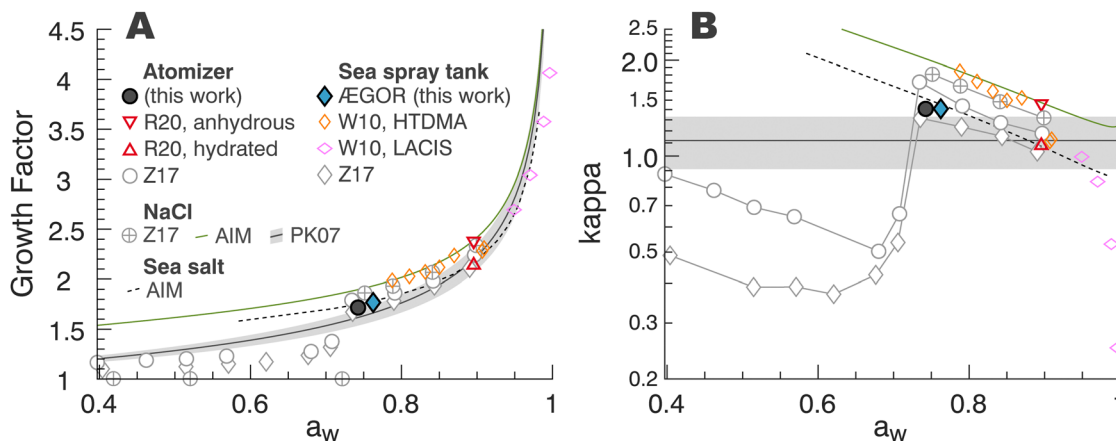


Fig. 5 (A) Sea salt growth factor as a function of water activity compared to other studies. W10 is Wex *et al.*, 2010. Z17 is Zieger *et al.*, 2017. R20 is Rosati *et al.*, 2020. PK07 is Petters and Kreidenweis, 2007. AIM is the Aerosol Inorganics Model (<https://www.aim.env.uea.ac.uk/aim/aim.php>).<sup>57,60</sup> The AIM calculation for sea salt was initialized using the exact composition used in this work (with  $\text{Br}^-$  replaced by  $\text{Cl}^-$ ). The NaCl measurement of Zieger *et al.* is from atomization. (B) Growth factor derived hygroscopicity. The dry NaCl (Z17 in panel A at  $a_w < 0.75$ ) was below the kappa range and is not shown.

differences could be more conclusively attributed to differences in spray generation methods if an intercomparison were performed using the same synthetic sea salt solution.

The growth factor of NaCl aerosol recommended by Petters and Kreidenweis<sup>43</sup> (PK07) is shown as grey shading. This range is based on observations and is converted to a growth factor for this work (panel A) using the published range in recommended  $\kappa$  values (panel B). The growth factor of pure NaCl predicted by AIM<sup>37</sup> is a little higher than the PK07 model, especially for lower water activities. The hygroscopic growth measurements (panel A) and  $\kappa$  values (panel B) of sea salt aerosols fall between these predictions for NaCl, likely due to the high fraction of NaCl within the sea salt mixture.

Hydrated forms of  $\text{MgCl}_2$  and  $\text{CaCl}_2$  may be present after complete drying the sea salt particles, retaining 5 to 14% greater volume as bound water than their anhydrous forms.<sup>59</sup> The bound water can be removed upon heating of the aerosol.<sup>33</sup> Measurement artifacts may also arise in other cases where the mobility-equivalent diameter selected by the first DMA is not equivalent to the mass-equivalent diameter, such as when the particles are non-spherical or porous.<sup>61,62</sup> Rosati *et al.*<sup>59</sup> recommend a hygroscopic growth factor and hygroscopicity for fully hydrated and fully anhydrous sea salt (plotted in Fig. 5, red triangles). The recommended range encompasses the range observed by several sources including this work.

Sea salt begins taking up trace amounts of water below its deliquescence point at an RH of 74%,<sup>63</sup> and the deliquescence point of the sea salt is evident in Fig. 5 (panel A) just above an  $a_w$  of 0.7. The dry salt measurement greatly reduces the apparent  $\kappa$  value plotted in panel B at  $a_w < 0.66$ . Above an  $a_w$  of 0.66, the  $\kappa$  values sharply rise in response to pre-deliquescent water uptake. Water uptake prior to deliquescence occurs due to hydration of the  $\text{MgCl}_2$  and  $\text{CaCl}_2$  salts<sup>63</sup> and can begin as surface accommodation of water on NaCl.<sup>64</sup> The measurements by Wex *et al.*<sup>58</sup> for sea salt aerosol generated by a sea spray tank are higher when measured by an HTDMA, and lower when

measured by the Leipzig Aerosol Cloud Interaction Simulator (LACIS).<sup>65</sup> Interestingly, the LACIS-derived  $\kappa$  value of sea salt is lower compared to values derived by other techniques, perhaps due to the optical detection method for the particles.<sup>65</sup>

### 3.3 Coating thickness of nanoplastic aerosols

Fig. 6, panel A shows the hygroscopic growth factor of salt coated PSL as a function of exponentially increasing salinity. The blue and grey shadings indicate the measurements performed without any salt in the bulk solution, showing growth factors very close to 1 below which coating cannot be detected. A measurable increase in water uptake by the nanoplastics is observed above a salinity of about  $0.1 \text{ g kg}^{-1}$ .

Note that the growth factor is measured for the wet particle, which ranges in size from 150 to 260 nm, and is fitted to a precision of  $\pm 1 \text{ nm}$  (increments of 0.01 in GF). This corresponds to a  $\Delta\tau$  ranging from  $\pm 0.07 \text{ nm}$  (at  $\text{GF} = 1.01$ ) to  $\pm 0.15 \text{ nm}$  (at  $\text{GF} = 1.80$ ). The width of the DMA transfer function is much larger, ranging from  $\pm 15 \text{ nm}$  at 150 nm to  $\pm 25 \text{ nm}$  at 260 nm (corresponding to  $\Delta\tau$  range of  $\pm 0.9$  to  $\pm 3.7 \text{ nm}$ ). The uncertainty of the coating thickness is likely between these extremes.

Fig. 6, panel B shows the coating thickness (in nm) and mass (in femtograms) of sea salt on PSL as a function of increasing salinity between  $10^{-3}$  and  $1 \text{ g kg}^{-1}$ , as calculated for the inverted size distributions following eqn (1)–(5). The AEGOR sea spray tank appears to produce thinner salt coating on the PSL particles than the atomizer. Future investigation of this trend could shed light on the differences between these two aerosol generation methods. Coating thickness increases with increasing salinity following a power law described by  $\log_{10}\tau = 0.29 \log_{10}s + 0.43$ , where  $\tau$  is expressed in nm and  $s$  in  $\text{g kg}^{-1}$ .

Fig. 6, panel C shows the size of droplets containing the nanoplastics, as calculated following eqn (7). The droplet size decreased with increasing salinity, following a power law described by  $\log_{10}D_{\text{drop}} = -0.23 \log_{10}s - 0.031$ , where  $D_{\text{drop}}$  is

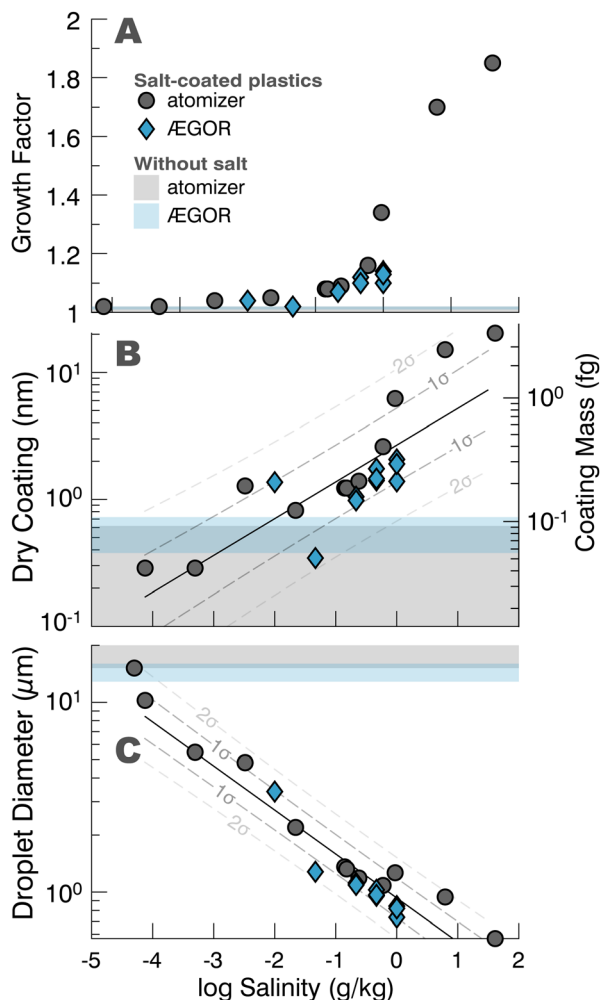


Fig. 6 (A) Polystyrene latex spheres' growth factors as a function of increasing salinity. Shadings indicate the level of water uptake in experiments without salt. (B) Coating thickness of dry sea salt on 147 nm polystyrene latex nanospheres as a function of bulk water salinity. Shading indicates the background level of coating. (C) Droplet size prior to evaporation. PSL content is 0.18 mg kg<sup>-1</sup> (circles) and 0.15 mg kg<sup>-1</sup> (diamonds). Note the log scale of the y-axis. Size selection was performed at 150 nm. Data are tabulated in Table S10 (ESI†). The black lines in panels B and C are fit to the data and the dotted lines are the 68% (1σ) and 95% (2σ) confidence intervals of the fit.

the droplet diameter expressed in μm and *s* is expressed in g kg<sup>-1</sup>. Droplets were generally at least a factor of 1000 times larger in diameter than the dried aerosols. The increasing droplet size with lower salinity is a result of the constant size selection at 150 nm in DMA 1. The plotted droplets therefore reflect the size of a liquid droplet collapsing with evaporation to a 150 nm dry diameter.

Fig. 6 also shows the comparison of the atomizer and ÆGOR sea spray tank aerosols. Although the Collison atomizer has often been used to generate sea salt aerosol,<sup>62,66–70</sup> in the marine boundary layer sea spray aerosol is generated by bubble bursting, which is more accurately simulated using a sea spray tank.<sup>31,71–73</sup> For the same water salinity, the PSL-containing particles from the ÆGOR tank were slightly smaller than those

generated by the atomizer, and thus the expectation is that these dried particles will have smaller coatings.

The PToF measurement (eqn (8)) enabled measurement of the Jayne shape factor, which was found here to be between 1 and 1.04 for the PSL peak, and between 0.99 and 1.16 for the sea salt peak. Water is not retained after passage through two dryers and the aerodynamic lens, and both salt and plastic peaks were detected at their dried-down diameters close to the sphere-equivalent 150 nm. The shape factors were found close to the expected values of between 1.08 and 1.12 for pure NaCl<sup>51,52,62,74</sup> and 1 for pure PSL. The PToF measurement performs best with larger particles than the 150 nm particles used in this study; because of this and the very reasonable shape factor estimate, we do not explore the shape factor further.

### 3.4 HTDMA-AMS spectra

Fig. 7 shows the overlay of the AMS-derived ion count as a function of humidified diameter and the HTDMA-derived particle and mass counts. Panel C shows the clear separation of small and large particles at 75% RH, similar to Fig. 2 and 3 and with similar resolution. These data were obtained in HTDMA mode prior to instrument switching into HTDMA-AMS mode.

Fig. 7, panel B shows the conversion of these particle number concentrations to particulate mass concentration (assuming a

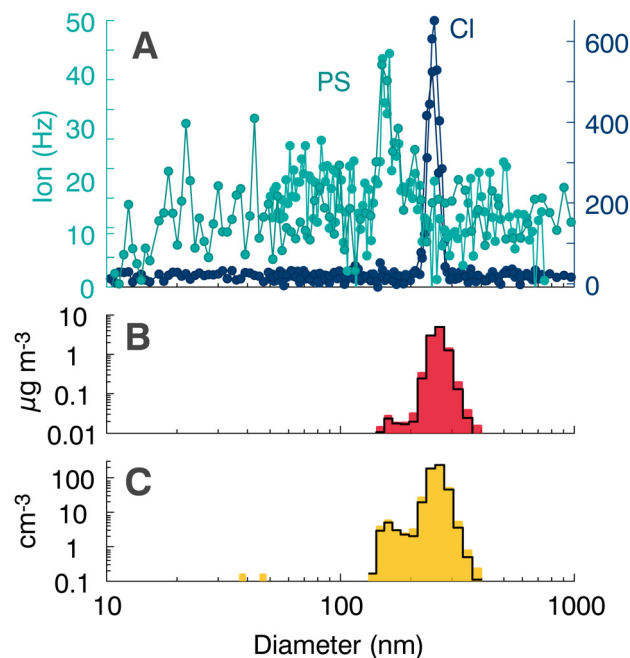


Fig. 7 Overlay of two repeated HTDMA-AMS scans aligned to the HTDMA diameter axis give scan times and rates. (A) AMS signal in units of ions per second for the polystyrene (PS) family of ions (*m/z* 104, 103, and 78; turquoise) and for the chloride (Cl) family of ions (dark blue). Experiments are included in Table S1 (ESI†) (#53 and 54). (B) Particulate mass as reported by the HTDMA. (C) Particle count reported by the HTDMA. (Experiment #51). Note that the size distribution is not inverted and has units of particles per cm<sup>3</sup>.



**Table 2** Ionization efficiencies of major ions in our experiments, flow rate to AMS 0.0980838 L min<sup>-1</sup>. Collection efficiency is assumed to be 0.25 for salt-coated PSL and for chloride

Species	Ions, <i>m/z</i>	<i>M<sub>w</sub></i> (g mol <sup>-1</sup> )	IE	RIE
Polystyrene	C <sub>8</sub> H <sub>8</sub> <sup>+</sup>	104, 103, 78	1.2417 × 10 <sup>-8</sup> <sup>a</sup>	0.19
Chloride	<sup>35</sup> Cl <sup>+</sup> , H <sup>35</sup> Cl <sup>+</sup> , <sup>37</sup> Cl <sup>+</sup> , H <sup>37</sup> Cl <sup>+</sup> , Na <sup>35</sup> Cl <sup>+</sup>	35, 36, 37, 38, 58	7.8896 × 10 <sup>-9</sup>	0.36

<sup>a</sup> Per monomer of *m/z* 104.0649.

density of NaCl throughout,  $\rho = 2.16 \text{ g cm}^{-3}$ . Assuming a density of  $1.05 \text{ g cm}^{-3}$  for PSL reduces the height of the PSL peak to  $0.011 \mu\text{g m}^{-3}$ . As could be expected, the smaller peak containing 150 nm particles is significantly more difficult to detect using the mass-based measurement. The peaks in mass concentration do not shift relative to the peaks in number concentration.

Fig. 7, panel A shows the extracted ion chromatograms of the high-resolution AMS signal after alignment to the HTDMA diameter axis. The peak in the styrene signal identifies the smaller particles as nanoplastics and the peak in sea salt ions identifies the larger peak as sea salt. These data were obtained in HTDMA-AMS mode with scan durations of up to two hours. The increase in scan time affords a higher signal-to-noise ratio, which was observed to be more important for the HTDMA-AMS measurements than for the HTDMA alone. These data are displayed as a timeseries in Fig. S2 (polystyrene) and S3 (sea salt chloride) in the ESI<sup>†</sup> and the signal-to-noise ratios of these peaks to the background AMS signal are tabulated in Tables S5 and S6 (ESI<sup>†</sup>).

Fig. 7 shows that the separation of the particles upstream of the AMS by their differential hygroscopicity can aid in the identification of plastics or other nanoparticles in the sea salt mixture. TDMA techniques are versatile and have been used to probe hygroscopicity<sup>44,45,75–77</sup> and volatility distributions<sup>75,78,79</sup> and measure viscosity.<sup>80,81</sup> Coupled with the AMS, the HTDMA technique has been used to characterize the hygroscopicity-resolved composition of the components of biomass burning smoke.<sup>77</sup> Upstream separation of particles by TDMA prior to the AMS also opens the possibility for volatility- or viscosity-resolved measurements that would aid in the interpretation of the AMS spectra.

### 3.5 Ionization efficiency

Table 2 shows the ionization efficiencies for sea salt chloride and for polystyrene, which are described further in the ESI<sup>†</sup> (Section S4). The RIE of sea salt chloride was 0.358, somewhat lower than that reported for chloride in the AMS characterization.<sup>82</sup> This is likely due to the refractory nature of NaCl,<sup>83</sup> and occurs despite raising the vaporizer temperature to 800 °C. Likewise, the RIE of polystyrene, quantified relative to the monomer, was 0.190, lower than the recommended RIE of 1.4 for organics,<sup>82</sup> also due to the refractory nature of the polymer. An elevated background signal associated with the slow desorption of NaCl complicates the analysis of sea salt by electron impact ionization techniques.

## 4 Conclusions

In this work, sea salt coating on polystyrene nanoplastics is observed and probed as a function of aerosol generation

methods including a Collision atomizer and the ÆGOR sea spray generation tank at Aarhus University in Denmark. Growth factor inversion was performed to calculate salt coating thicknesses between 0.5 and 5 nm for salinities ranging from  $3 \times 10^{-3}$  to  $1 \text{ g kg}^{-1}$ . Coating on 150 nm polystyrene latex spheres increased with increasing salinity following a power law, and the atomizer was observed to produce thicker salt coatings than the sea spray tank. A hygroscopicity TDMA (HTDMA) instrument was used at 75% RH for online separation of nanoplastic aerosol from the sea spray aerosol. Clear separation of the airborne sea salt particles from the nanoplastics was achieved for salinities up to  $6 \text{ g kg}^{-1}$ . Hygroscopic growth factors for polystyrene latex were approximately 1, but increased with increasing salinity. The sea salt growth factor was 1.74 and its hygroscopicity parameter ( $\kappa$ ) was 1.41, in agreement with previous studies of sea salt and very close to the range established for pure NaCl. HTDMA-separated aerosol was routed to an HR-ToF-AMS to obtain hygroscopicity-resolved mass spectra, using an elevated vaporizer temperature to evaporate the (semi-)refractory NaCl and polystyrene particles. After applying a collection efficiency of 0.25 (based on the salt or salt-coated surfaces), the relative ionization efficiencies at 800 °C of sea salt chloride and salt-coated polystyrene latex were found to be 0.36 and 0.19, respectively.

It seems clear that atmospheric nanoplastic aerosols from sea spray generation will be accompanied by sea salt.<sup>1,9</sup> Our results demonstrate the power-law dependence of nanoplastic salt coating thickness on bulk salinity for bubble-bursting aerosol and pneumatically atomized aerosols using online separation of airborne nanoplastics from sea salt particles coupled to detailed characterization by aerosol mass spectrometry. Sea salt coatings found on nanoplastic particles increased in thickness exponentially with increasing bulk water salinity. The mechanism of bubble bursting and aerosol release is shown to be influenced by the bulk solution salinity.

Surface coatings on particles impact their optical properties because the thin layer of salt encourages water uptake; this impacts global climate, and visibility in the boundary layer. Salt coating also dilutes other coatings that may be present, shifting the equilibrium composition and activity of solution. Solution activity is a controlling factor in heterogeneous reaction rates of atmospheric aerosols. Further investigation of nanoplastic surfaces will be necessary to understand the impact of environmental conditions on aerosolized nanoplastic water uptake, surface chemistry, and size distribution dynamics in the atmosphere.

## Conflicts of interest

There are no conflicts to declare.

## Acknowledgements

This work was supported by the Independent Research Fund Denmark (grant number 0217-00442B). Lærke Sloth Nielsen is acknowledged for assistance with the HTDMA. We thank the Villum Foundation for supporting the original purchase of the HTDMA instrument (Villum Research Station, Grant Number: VKR023001). We acknowledge support from the Danish National Research Foundation (DNRF172) through the Center for Chemistry of Clouds. Pedro Compuzano-Jost is acknowledged for helpful comments on AMS data processing. Mads Mørk Jensen, Emil Iversen, and Ditte Thomsen are acknowledged for technical assistance with the AMS.

## Notes and references

- 1 D. K. A. Barnes, F. Galgani, R. C. Thompson and M. Barlaz, Accumulation and fragmentation of plastic debris in global environments, *Philos. Trans. R. Soc., B*, 2009, **364**, 1985–1998.
- 2 E. van Sebille, The oceans' accumulating plastic garbage, *Phys. Today*, 2015, **68**, 60–61.
- 3 E. Besseling, B. Wang, M. Lüring and A. A. Koelmans, Nanoplastic Affects Growth of *S. obliquus* and Reproduction of *D. magna*, *Environ. Sci. Technol.*, 2014, **48**, 12336–12343.
- 4 R. H. Waring, R. M. Harris and S. C. Mitchell, Plastic contamination of the food chain: A threat to human health?, *Maturitas*, 2018, **115**, 64–68.
- 5 K. E. Goodman, J. T. Hare, Z. I. Khamis, T. Hua and Q.-X. A. Sang, Exposure of Human Lung Cells to Polystyrene Microplastics Significantly Retards Cell Proliferation and Triggers Morphological Changes, *Chem. Res. Toxicol.*, 2021, **34**, 1069–1081.
- 6 I. Jakubowicz, J. Enebro and N. Yarahmadi, Challenges in the search for nanoplastics in the environment – A critical review from the polymer science perspective, *Polym. Test.*, 2021, **93**, 106953.
- 7 J. Gigault, A. ter Halle, M. Baudrimont, P.-Y. Pascal, F. Gauffre, T.-L. Phi, H. El Hadri, B. Grassl and S. Reynaud, Current opinion: What is a nanoplastic?, *Environ. Poll.*, 2018, **235**, 1030–1034.
- 8 A. ter Halle and J. F. Ghiglione, Nanoplastics: A Complex, Polluting Terra Incognita, *Environ. Sci. Technol.*, 2021, **55**, 14466–14469.
- 9 A. A. Koelmans, E. Besseling and W. J. Shim, in *Marine Anthropogenic Litter*, ed. M. Bergmann, L. Gutow and M. Klages, Springer International Publishing, Cham, 2015, pp. 325–340.
- 10 P. A. Stapleton, Toxicological considerations of nano-sized plastics, *AIMS Environ. Sci.*, 2019, **6**, 367–378.
- 11 R. C. Thompson, Y. Olsen, R. P. Mitchell, A. Davis, S. J. Rowland, A. W. G. John, D. McGonigle and A. E. Russell, Lost at Sea: Where Is All the Plastic?, *Science*, 2004, **304**, 838.
- 12 A. Cózar, F. Echevarría, J. I. González-Gordillo, X. Irigoien, B. Úbeda, S. Hernández-León, A. T. Palma, S. Navarro, J. García-de-Lomas, A. Ruiz, M. L. Fernández-de-Puelles and C. M. Duarte, Plastic debris in the open ocean, *Proc. Natl. Acad. Sci. U. S. A.*, 2014, **111**, 10239–10244.
- 13 S. Allen, D. Allen, K. Moss, G. Le Roux, V. R. Phoenix and J. E. Sonke, Examination of the ocean as a source for atmospheric microplastics, *PLoS One*, 2020, **15**, e0232746.
- 14 M. Trainic, J. M. Flores, I. Pinkas, M. L. Pedrotti, F. Lombard, G. Bourdin, G. Gorsky, E. Boss, Y. Rudich, A. Vardi and I. Koren, Airborne microplastic particles detected in the remote marine atmosphere, *Commun. Earth Environ.*, 2020, **1**, 64.
- 15 E. Kjærgaard, F. Hasager, S. S. Petters, M. Glasius and M. Bilde, Bubble-Mediated Generation of Airborne Nanoplastic Particles, 2023, submitted.
- 16 Y. Wang, H. Okochi, Y. Tani, H. Hayami, Y. Minami, N. Katsumi, M. Takeuchi, A. Sorimachi, Y. Fujii, M. Kajino, K. Adachi, Y. Ishihara, Y. Iwamoto and Y. Niida, Airborne hydrophilic microplastics in cloud water at high altitudes and their role in cloud formation, *Environ. Chem. Lett.*, 2023, **21**, 3055–3062.
- 17 P. F. DeCarlo, J. R. Kimmel, A. Trimborn, M. J. Northway, J. T. Jayne, A. C. Aiken, M. Gonin, K. Fuhrer, T. Horvath, K. S. Docherty, D. R. Worsnop and J. L. Jimenez, Field-Deployable, High-Resolution, Time-of-Flight Aerosol Mass Spectrometer, *Anal. Chem.*, 2006, **78**, 8281–8289.
- 18 J. Ovadnevaite, D. Ceburnis, M. Canagaratna, H. Berresheim, J. Bialek, G. Martucci, D. R. Worsnop and C. O'Dowd, On the effect of wind speed on submicron sea salt mass concentrations and source fluxes, *J. Geophys. Res.: Atmos.*, 2012, **117**, D16201.
- 19 S. M. Pieber, I. El Haddad, J. G. Slowik, M. R. Canagaratna, J. T. Jayne, S. M. Platt, C. Bozzetti, K. R. Daellenbach, R. Fröhlich, A. Vlachou, F. Klein, J. Dommen, B. Miljevic, J. L. Jiménez, D. R. Worsnop, U. Baltensperger and A. S. H. Prévôt, Inorganic Salt Interference on CO<sup>2+</sup> in Aerodyne AMS and ACSM Organic Aerosol Composition Studies, *Environ. Sci. Technol.*, 2016, **50**, 10494–10503.
- 20 D. K. Farmer, A. Matsunaga, K. S. Docherty, J. D. Surratt, J. H. Seinfeld, P. J. Ziemann and J. L. Jimenez, Response of an aerosol mass spectrometer to organonitrates and organosulfates and implications for atmospheric chemistry, *Proc. Natl. Acad. Sci. U. S. A.*, 2010, **107**, 6670–6675.
- 21 O. Laskina, H. S. Morris, J. R. Grandquist, Z. Qin, E. A. Stone, A. V. Tivanski and V. H. Grassian, Size Matters in the Water Uptake and Hygroscopic Growth of Atmospherically Relevant Multicomponent Aerosol Particles, *J. Phys. Chem. A*, 2015, **119**, 4489–4497.
- 22 S. S. Petters, Constraints on the role of Laplace pressure in multiphase reactions and viscosity of organic aerosols, *Geophys. Res. Lett.*, 2022, **49**, e2022GL098959.
- 23 A. Haider and O. Levenspiel, Drag coefficient and terminal velocity of spherical and nonspherical particles, *Powder Technol.*, 1989, **58**, 63–70.
- 24 S. Zellnitz, L. Zellnitz, M. T. Müller, C. Meindl, H. Schröttner and E. Fröhlich, Impact of drug particle shape on permeability and cellular uptake in the lung, *Eur. J. Pharm. Sci.*, 2019, **139**, 105065.

- 25 M. C. Rillig, A. Lehmann, M. Ryo and J. Bergmann, Shaping Up: Toward Considering the Shape and Form of Pollutants, *Environ. Sci. Technol.*, 2019, **53**, 7925–7926.
- 26 H. Xue, A. F. Khalizov, L. Wang, J. Zheng and R. Zhang, Effects of dicarboxylic acid coating on the optical properties of soot, *Phys. Chem. Chem. Phys.*, 2009, **11**, 7869–7875.
- 27 E. Loukhovitskaya, Y. Bedjanian, I. Morozov and G. Le Bras, Laboratory study of the interaction of HO<sub>2</sub> radicals with the NaCl, NaBr, MgCl<sub>2</sub>·6H<sub>2</sub>O and sea salt surfaces, *Phys. Chem. Chem. Phys.*, 2009, **11**, 7896–7905.
- 28 I. Unger, C.-M. Saak, M. Salter, P. Zieger, M. Patanen and O. Björneholm, Influence of Organic Acids on the Surface Composition of Sea Spray Aerosol, *J. Phys. Chem. A*, 2020, **124**, 422–429.
- 29 O. S. Ryder, N. R. Campbell, H. Morris, S. Forestieri, M. J. Ruppel, C. Cappa, A. Tivanski, K. Prather and T. H. Bertram, Role of Organic Coatings in Regulating N<sub>2</sub>O<sub>5</sub> Reactive Uptake to Sea Spray Aerosol, *J. Phys. Chem. A*, 2015, **119**, 11683–11692.
- 30 L. S. Nielsen and M. Bilde, Exploring controlling factors for sea spray aerosol production: temperature, inorganic ions and organic surfactants, *Tellus B*, 2020, **72**, 1–10.
- 31 S. Christiansen, M. E. Salter, E. Gorokhova, Q. T. Nguyen and M. Bilde, Sea Spray Aerosol Formation: Laboratory Results on the Role of Air Entrainment, Water Temperature, and Phytoplankton Biomass, *Environ. Sci. Technol.*, 2019, **53**, 13107–13116.
- 32 S. M. King, A. C. Butcher, T. Rosenoern, E. Coz, K. I. Lieke, G. de Leeuw, E. D. Nilsson and M. Bilde, Investigating Primary Marine Aerosol Properties: CCN Activity of Sea Salt and Mixed Inorganic–Organic Particles, *Environ. Sci. Technol.*, 2012, **46**, 10405–10412.
- 33 B. B. Rasmussen, Q. T. Nguyen, K. Kristensen, L. S. Nielsen and M. Bilde, What controls volatility of sea spray aerosol? Results from laboratory studies using artificial and real seawater samples, *J. Aerosol Sci.*, 2017, **107**, 134–141.
- 34 X. Lopez-Yglesias, M. C. Yeung, S. E. Dey, F. J. Brechtel and C. K. Chan, Performance Evaluation of the Brechtel Mfg. Humidified Tandem Differential Mobility Analyzer (BMI HTDMA) for Studying Hygroscopic Properties of Aerosol Particles, *Aerosol Sci. Technol.*, 2014, **48**, 969–980.
- 35 B. Rosati, S. Isokääntä, S. Christiansen, M. M. Jensen, S. P. Moosakutty, R. Wollesen de Jonge, A. Massling, M. Glasius, J. Elm, A. Virtanen and M. Bilde, Hygroscopicity and CCN potential of DMS-derived aerosol particles, *Atmos. Chem. Phys.*, 2022, **22**, 13449–13466.
- 36 A. Massling, R. Lange, J. B. Pernov, U. Gosewinkel, L.-L. Sørensen and H. Skov, Measurement report: High Arctic aerosol hygroscopicity at sub- and supersaturated conditions during spring and summer, *Atmos. Chem. Phys.*, 2023, **23**, 4931–4953.
- 37 L. Williams, What is My Vaporizer Temperature? 11th AMS Users Meeting, Hyytiälä, Finland, 2010, [https://cires1.colorado.edu/jimenez-group/UsrMtg/UsersMtg11/WilliamsAMUsersMtg\\_2010\\_VapT.pdf](https://cires1.colorado.edu/jimenez-group/UsrMtg/UsersMtg11/WilliamsAMUsersMtg_2010_VapT.pdf), Retrieved 10-Oct-2023.
- 38 W. Hu, P. Campuzano-Jost, D. A. Day, P. Croteau, M. R. Canagaratna, J. T. Jayne, D. R. Worsnop and J. L. Jimenez, Evaluation of the new capture vaporizer for aerosol mass spectrometers (AMS) through field studies of inorganic species, *Aerosol Sci. Technol.*, 2017, **51**, 735–754.
- 39 S. R. Suda, M. D. Petters, A. Matsunaga, R. C. Sullivan, P. J. Ziemann and S. M. Kreidenweis, Hygroscopicity frequency distributions of secondary organic aerosols, *J. Geophys. Res.: Atmos.*, 2012, **117**, D04207.
- 40 S. C. Wang and R. C. Flagan, Scanning electrical mobility spectrometer, *Aerosol Sci. Technol.*, 1990, **13**, 230–240.
- 41 M. D. Petters, A language to simplify computation of differential mobility analyzer response functions, *Aerosol Sci. Technol.*, 2018, **52**, 1437–1451.
- 42 M. D. Petters, Revisiting matrix-based inversion of scanning mobility particle sizer (SMPS) and humidified tandem differential mobility analyzer (HTDMA) data, *Atmos. Meas. Tech.*, 2021, **14**, 7909–7928.
- 43 M. D. Petters and S. M. Kreidenweis, A single parameter representation of hygroscopic growth and cloud condensation nucleus activity, *Atmos. Chem. Phys.*, 2007, **7**, 1961–1971.
- 44 B. Rosati, S. Christiansen, A. Dinesen, P. Roldin, A. Massling, E. D. Nilsson and M. Bilde, The impact of atmospheric oxidation on hygroscopicity and cloud droplet activation of inorganic sea spray aerosol, *Sci. Rep.*, 2021, **11**, 10008.
- 45 S. R. Suda and M. D. Petters, Accurate determination of aerosol activity coefficients at relative humidities up to 99% using the hygroscopicity tandem differential mobility analyzer technique, *Aerosol Sci. Technol.*, 2013, **47**, 991–1000.
- 46 D. Sueper and collaborators, ToF-AMS Data Analysis Software Webpage, [https://cires1.colorado.edu/jimenez-group/wiki/index.php/ToF-AMS\\_Analysis\\_Software](https://cires1.colorado.edu/jimenez-group/wiki/index.php/ToF-AMS_Analysis_Software). Accessed July 2023.
- 47 J. C. Corbin, A. Othman, J. D. Allan, D. R. Worsnop, J. D. Haskins, B. Sierau, U. Lohmann and A. A. Mensah, Peak-fitting and integration imprecision in the Aerodyne aerosol mass spectrometer: effects of mass accuracy on location-constrained fits, *Atmos. Meas. Tech.*, 2015, **8**, 4615–4636.
- 48 P. O. Momoh, A. M. Hamid, A.-R. Soliman, S. A. Abrash and M. S. El-Shall, Structure of the C<sub>8</sub>H<sub>8</sub><sup>+</sup> Radical Cation Formed by Electron Impact Ionization of Acetylene Clusters. Evidence for a (Benzene<sup>+</sup>-Acetylene) Complex, *J. Phys. Chem. Lett.*, 2011, **2**, 2412–2419.
- 49 F. Hasager, S. F. Vinter, Þ. Björgvinsdóttir, E. R. Kjærgaard, S. S. Petters, M. Bilde and M. Glasius, Optimization and application of an analytical pyrolysis method for detection of airborne polystyrene nanoparticles, *J. Chromatogr. A*, DOI: [10.2139/ssrn.4459268](https://doi.org/10.2139/ssrn.4459268).
- 50 *NIST Chemistry WebBook - Standard Reference Data Number 69*, ed. P. J. Linstrom and W. G. Mallard, National Institute of Standards and Technology, 2017, <https://doi.org/10.18434/T4D303> (retrieved April 30, 2022).
- 51 J. T. Jayne, D. C. Leard, X. Zhang, P. Davidovits, K. A. Smith, C. E. Kolb and D. R. Worsnop, Development of an Aerosol Mass Spectrometer for Size and Composition Analysis of Submicron Particles, *Aerosol Sci. Technol.*, 2000, **33**, 49–70.
- 52 P. F. DeCarlo, J. G. Slowik, D. R. Worsnop, P. Davidovits and J. L. Jimenez, Particle morphology and density characterization

- by combined mobility and aerodynamic diameter measurements. Part 1: Theory, *Aerosol Sci. Technol.*, 2004, **38**, 1185–1205.
- 53 M. A. Browne, Sources and Pathways of Microplastics to Habitats, in *Marine Anthropogenic Litter*, ed. M. Bergmann, L. Gutow and M. Klages, Springer International Publishing, 2015, pp. 229–244.
- 54 Global Ocean Physics Analysis and Forecast, E.U. Copernicus Marine Service Information (CMEMS), Marine Data Store (MDS), DOI: [10.48670/moi-00016](https://doi.org/10.48670/moi-00016), Retrieved 01-May-2022.
- 55 E. van Sebille, C. Wilcox, L. Lebreton, N. Maximenko, B. D. Hardesty, J. A. van Franeker, M. Eriksen, D. Siegel, F. Galgani and K. L. Law, A global inventory of small floating plastic debris, *Environ. Res. Lett.*, 2015, **10**, 124006.
- 56 P. Zieger, O. Väisänen, J. C. Corbin, D. G. Partridge, S. Bastelberger, M. Mousavi-Fard, B. Rosati, M. Gysel, U. K. Krieger, C. Leck, A. Nenes, I. Riipinen, A. Virtanen and M. E. Salter, Revising the hygroscopicity of inorganic sea salt particles, *Nature Commun.*, 2017, **8**, 15883.
- 57 S. L. Clegg, P. Brimblecombe and A. S. Wexler, Thermodynamic model of the system  $\text{H}^+ - \text{NH}_4^+ - \text{Na}^+ - \text{SO}_4^{2-} - \text{NO}_3^- - \text{Cl}^- - \text{H}_2\text{O}$  at 298.15 K, *J. Phys. Chem. A*, 1998, **102**, 2155–2171.
- 58 H. Wex, E. Fuentes, G. Tsagkogeorgas, J. Voigtländer, T. Clauss, A. Kiselev, D. H. Green, H. Coe, G. McFiggans and F. Stratmann, The Influence of Algal Exudate on the Hygroscopicity of Sea Spray Particles, *Adv. Meteorol.*, 2010, **2010**, 365131.
- 59 B. Rosati, A. Paul, E. M. Iversen, A. Massling and M. Bilde, Reconciling atmospheric water uptake by hydrate forming salts, *Environ. Sci.: Process. Impacts*, 2020, **22**, 1759–1767.
- 60 A. S. Wexler and S. L. Clegg, Atmospheric aerosol models for systems including the ions  $\text{H}^+$ ,  $\text{NH}_4^+$ ,  $\text{Na}^+$ ,  $\text{SO}_4^{2-}$ ,  $\text{NO}_3^-$ ,  $\text{Cl}^-$ ,  $\text{Br}^-$ , and  $\text{H}_2\text{O}$ , *J. Geophys. Res.*, 2002, **107**, 4207.
- 61 S. Nakao, S. R. Suda, M. Camp, M. D. Petters and S. M. Kreidenweis, Droplet activation of wet particles: development of the Wet CCN approach, *Atmos. Meas. Tech.*, 2014, **7**, 2227–2241.
- 62 S. S. Petters and M. D. Petters, Surfactant effect on cloud condensation nuclei for two-component internally mixed aerosols, *J. Geophys. Res.-Atmos.*, 2016, **121**, 1878–1895.
- 63 I. N. Tang, A. C. Tridico and K. H. Fung, Thermodynamic and optical properties of sea salt aerosols, *J. Geophys. Res.-Atmos.*, 1997, **102**, 23269–23275.
- 64 J. J. Lin, K. Raj R, S. Wang, E. Kokkonen, M.-H. Mikkilä, S. Urpelainen and N. L. Prisle, Pre-deliquescent water uptake in deposited nanoparticles observed with in situ ambient pressure X-ray photoelectron spectroscopy, *Atmos. Chem. Phys.*, 2021, **21**, 4709–4727.
- 65 A. Kiselev, H. Wex, F. Stratmann, A. Nadeev and D. Karpushenko, White-light optical particle spectrometer for in situ measurements of condensational growth of aerosol particles, *Appl. Opt.*, 2005, **44**, 4693–4701.
- 66 D. D. Weis and G. E. Ewing, Water content and morphology of sodium chloride aerosol particles, *J. Geophys. Res.*, 1999, **104**, 21275–21285.
- 67 D. J. Cziczo and J. P. D. Abbatt, Infrared Observations of the Response of NaCl,  $\text{MgCl}_2$ ,  $\text{NH}_4\text{HSO}_4$ , and  $\text{NH}_4\text{NO}_3$  Aerosols to Changes in Relative Humidity from 298 to 238 K, *J. Phys. Chem. A*, 2000, **104**, 2038–2047.
- 68 T. B. Kristensen, N. L. Prisle and M. Bilde, Cloud droplet activation of mixed model HULIS and NaCl particles: Experimental results and  $\kappa$ -Köhler theory, *Atmos. Res.*, 2014, **137**, 167–175.
- 69 S. D. Forestieri, S. M. Staudt, T. M. Kuborn, K. Faber, C. R. Ruehl, T. H. Bertram and C. D. Cappa, Establishing the impact of model surfactants on cloud condensation nuclei activity of sea spray aerosol mimics, *Atmos. Chem. Phys.*, 2018, **18**, 10985–11005.
- 70 R. L. Bramblett and A. A. Frossard, Constraining the Effect of Surfactants on the Hygroscopic Growth of Model Sea Spray Aerosol Particles, *J. Phys. Chem. A*, 2022, **126**, 8695–8710.
- 71 K. A. Prather, T. H. Bertram, V. H. Grassian, G. B. Deane, M. D. Stokes, P. J. DeMott, L. I. Aluwihare, B. P. Palenik, F. Azam, J. H. Seinfeld, R. C. Moffet, M. J. Molina, C. D. Cappa, F. M. Geiger, G. C. Roberts, L. M. Russell, A. P. Ault, J. Baltrusaitis, D. B. Collins, C. E. Corrigan, L. A. Cuadra-Rodriguez, C. J. Ebben, S. D. Forestieri, T. L. Guasco, S. P. Hersey, M. J. Kim, W. F. Lambert, R. L. Modini, W. Mui, B. E. Pedler, M. J. Ruppel, O. S. Ryder, N. G. Schoepp, R. C. Sullivan and D. Zhao, Bringing the ocean into the laboratory to probe the chemical complexity of sea spray aerosol, *Proc. Natl. Acad. Sci. U. S. A.*, 2013, **110**, 7550–7555.
- 72 M. E. Salter, E. D. Nilsson, A. Butcher and M. Bilde, On the seawater temperature dependence of the sea spray aerosol generated by a continuous plunging jet, *J. Geophys. Res.: Atmos.*, 2014, **119**, 9052–9072.
- 73 N. L. Prisle, T. Raatikainen, R. Sorjamaa, B. Svenningsson, A. Laaksonen and M. Bilde, Surfactant partitioning in cloud droplet activation: a study of C8, C10, C12 and C14 normal fatty acid sodium salts, *Tellus, Ser. B*, 2008, **60**, 416–431.
- 74 G. Biskos, D. Paulsen, L. M. Russell, P. R. Buseck and S. T. Martin, Prompt deliquescence and efflorescence of aerosol nanoparticles, *Atmos. Chem. Phys.*, 2006, **6**, 4633–4642.
- 75 D. J. Rader and P. H. McMurry, Application of the tandem differential mobility analyzer to studies of droplet growth or evaporation, *J. Aerosol Sci.*, 1986, **17**, 771–787.
- 76 A. Massling, N. Niedermeier, T. Hennig, E. O. Fors, E. Swietlicki, M. Ehn, K. Hämeri, P. Villani, P. Laj, N. Good, G. B. McFiggans and A. Wiedensohler, Results and recommendations from an intercomparison of six Hygroscopicity-TDMA systems, *Atmos. Meas. Tech.*, 2011, **4**, 485–497.
- 77 M. I. Schurman, J. Y. Kim, H. H. Y. Cheung and C. K. Chan, Atmospheric particle composition-hygroscopic growth measurements using an in-series hybrid tandem differential mobility analyzer and aerosol mass spectrometer, *Aerosol Sci. Technol.*, 2017, **51**, 694–703.
- 78 M. Bilde, B. Svenningsson, J. Mønster and T. Rosenørn, Even–Odd Alternation of Evaporation Rates and Vapor Pressures of C3–C9 Dicarboxylic Acid Aerosols, *Environ. Sci. Technol.*, 2003, **37**, 1371–1378.
- 79 R. L. Modini, B. Harris and Z. D. Ristovski, The organic fraction of bubble-generated, accumulation mode Sea



- Spray Aerosol (SSA), *Atmos. Chem. Phys.*, 2010, **10**, 2867–2877.
- 80 N. E. Rothfuss and M. D. Petters, Characterization of the temperature and humidity-dependent phase diagram of amorphous nanoscale organic aerosols, *Phys. Chem. Chem. Phys.*, 2017, **19**, 6532–6545.
- 81 S. S. Petters, S. M. Kreidenweis, A. P. Grieshop, P. J. Ziemann and M. D. Petters, Temperature- and Humidity-Dependent Phase States of Secondary Organic Aerosols, *Geophys. Res. Lett.*, 2019, **46**(2), 1005–1013.
- 82 J. L. Jimenez, J. T. Jayne, Q. Shi, C. E. Kolb, D. R. Worsnop, I. Yourshaw, J. H. Seinfeld, R. C. Flagan, X. Zhang, K. A. Smith, J. W. Morris and P. Davidovits, Ambient aerosol sampling using the Aerodyne Aerosol Mass Spectrometer, *J. Geophys. Res.: Atmos.*, 2003, **108**, 8425, D7.
- 83 S. R. Zorn, F. Drewnick, M. Schott, T. Hoffmann and S. Borrmann, Characterization of the South Atlantic marine boundary layer aerosol using an aerodyne aerosol mass spectrometer, *Atmos. Chem. Phys.*, 2008, **8**, 4711–4728.